Nanoscale

PAPER

Cite this: *Nanoscale*, 2015, **7**, 18780

Enhancement of photodetection characteristics of MoS_2 field effect transistors using surface treatment with copper phthalocyanine†

Jinsu Pak,[a] Jingon Jang,[a] Kyungjune Cho,[a] Tae-Young Kim,[a] Jae-Keun Kim,[a] Younggul Song,[a] Woong-Ki Hong,*[b] Misook Min,*[a] Hyoyoung Lee[c] and Takhee Lee*[a]

Recently, two-dimensional materials such as molybdenum disulfide (MoS_2) have been extensively studied as channel materials for field effect transistors (FETs) because MoS_2 has outstanding electrical properties such as a low subthreshold swing value, a high on/off ratio, and good carrier mobility. In this study, we characterized the electrical and photo-responsive properties of MoS_2 FET when stacking a p-type organic copper phthalocyanine (CuPc) layer on the MoS_2 surface. We observed that the threshold voltage of MoS_2 FET could be controlled by stacking the CuPc layers due to a charge transfer phenomenon at the interface. Particularly, we demonstrated that CuPc/MoS_2 hybrid devices exhibited high performance as a photodetector compared with the pristine MoS_2 FETs, caused by more electron–hole pairs separation at the p–n interface. Furthermore, we found the optimized CuPc thickness (~2 nm) on the MoS_2 surface for the best performance as a photodetector with a photoresponsivity of ~1.98 A W^{-1}, a detectivity of ~6.11 × 10^{10} Jones, and an external quantum efficiency of ~12.57%. Our study suggests that the MoS_2 vertical hybrid structure with organic material can be promising as efficient photodetecting devices and optoelectronic circuits.

Received 20th July 2015,
Accepted 4th October 2015

DOI: 10.1039/c5nr04836b

www.rsc.org/nanoscale

Introduction

Recently, transition metal dichalcogenide (TMD) two-dimensional (2D) materials have gained considerable interest as a candidate for next-generation nanoelectronic devices.[1–6] TMD 2D materials have demonstrated several advantageous features, such as a thickness-dependent electronic band structure, high photoconductivity, high transparency, and flexibility in fabricating nanoelectronic devices. Among the various TMD materials, MoS_2 has been widely researched as a 2D FET and has exhibited outstanding electrical properties, including a low subthreshold swing value, a high on/off ratio, and good carrier mobility.[7–9] In contrast to graphene which lacks an energy band gap, MoS_2 has a direct band gap of 1.8 eV as a single layer and an indirect band gap of 1.2 eV as a bulk material.[10–14] Therefore, many studies have used MoS_2 to fabricate transistors,[15–18] memory,[19,20] logic circuit devices,[21,22] sensors,[23,24] and phototransistors.[25,27–29] Graphene has also been studied for phototransistors for application in photosensitive devices, but graphene-transistor-based photodetectors have a limited photoresponsivity (~6 mA W^{-1}) due to graphene's low light absorption coefficient and the fast photo-induced carrier recombination rate.[26] In contrast, photodetectors made with MoS_2 have exhibited excellent photoresponse properties. For example, devices based on single- and multilayer MoS_2 films have demonstrated photoresponsivities up to 880 A W^{-1} (ref. 27) and ~0.1 A W^{-1},[28,29] respectively.

Beyond the structures of MoS_2 FET alone, it has been demonstrated that through stacking of other materials, MoS_2-based heterostructures can result in higher photoresponsivity.[30–35] For example, Kufer *et al.* demonstrated that the photoresponsivity of MoS_2 was enhanced by stacking p-type PbS quantum dot materials on an MoS_2 surface due to the photo-generated charge transfer from the stacked p-type PbS quantums to MoS_2.[35] If p-type materials are to be used for heterostructure MoS_2-based photodetectors, organic materials can be a good choice because p-type organic semiconductor layers have been extensively studied and can be easily stacked

[a]*Department of Physics and Astronomy, and Institute of Applied Physics, Seoul National University, Seoul 08826, Korea. E-mail: minmi0924@gmail.com, tlee@snu.ac.kr*
[b]*Jeonju Center, Korea Basic Science Institute, Jeonju, Jeollabuk-do 54907, Korea. E-mail: wkh27@kbsi.re.kr*
[c]*Center for Integrated Nanostructure Physics, Institute for Basic Science (IBS), Department of Energy Science, Department of Chemistry, Sungkyunkwan University, Suwon 16410, Korea*

†Electronic supplementary information (ESI) available. See DOI: 10.1039/c5nr04836b

on 2D films by spin-coating or deposition systems, and the thickness of the organic layer on 2D films can be accurately controlled. Among organic materials, CuPc is a p-type organic semiconductor that has been widely used in organic and hybrid optoelectronic devices.[36] The structural properties of the CuPc layer on the MoS_2 surface have been studied. For example, molecular orientation properties of the CuPc layer on the MoS_2 were studied using angular resolved ultraviolet photoemission spectroscopy or atomic force microscopy,[37] and a Raman enhancement effect of the CuPc/MoS_2 was reported.[38] However, the effects of the CuPc hybrid structures on the MoS_2-based phototransistors have not yet been examined. Importantly, as the device consisted of a heterostructure with n-type MoS_2 and p-type CuPc materials, the efficiency of photoresponse can strongly depend on the thickness of the organic layer.

In this study, we have characterized the electrical and photoresponsive properties of MoS_2 FET-based photodetectors. We investigated and compared the photodetection characteristics of MoS_2 FET devices before and after the devices were stacked with p-type organic semiconductor (CuPc) layers on the MoS_2 surface. By varying the thickness of the CuPc layers, we found an optimized condition for achieving higher photoresponsivity in the CuPc/MoS_2 hybrid device structures.

Results and discussion

Fig. 1a shows the optical images of a MoS_2 flake and its device fabrication into a MoS_2 FET. Here, MoS_2 flakes were mechanically exfoliated from a bulk MoS_2 crystal (purchased from SPI Supplier, USA) and transferred onto a 270 nm-thick SiO_2 layer on a heavily doped p++ Si substrate that can be used as a back gate of FET devices. Then, Ti metal (30 nm thick) patterns were made into the source and drain electrodes using electron-beam lithography to form ohmic contacts, as shown in Fig. S1.† Since Ti electrode has a relatively lower work function (~4.3 eV) than the work function of MoS_2 (4.5 to 5.2 eV), it can form ohmic contact with MoS_2.[39] Detailed information on the device fabrication is explained in the ESI (Fig. S2†). Fig. 1b displays an atomic force microscopy (AFM) image of a MoS_2 FET. The thickness of the MoS_2 flake channel was found to be ~3.2 nm, corresponding to 5 layers of the MoS_2 film (the thickness of a single-layer MoS_2 film is 0.65 nm). We fabricated MoS_2 FETs using 3 to 6 nm-thick MoS_2 flakes, corresponding to 5 to 9 layers of MoS_2 films. After fabricating the MoS_2 FET devices, the CuPc organic material was deposited on the MoS_2 surface using a thermal evaporator. Fig. 1c illustrates the schematics of a CuPc/MoS_2 photodetector illuminated by a visible light laser. The molecular structures of the MoS_2 and CuPc are also shown in Fig. 1c.

First, we examined the stacking of CuPc layers on MoS_2 flakes by Raman spectroscopy. We observed that the MoS_2 flakes exhibited two Raman characteristic bands at 383 and 405 cm^{-1}, corresponding to out-of-plane (A_{1g} mode) and in-plane (E_{2g} mode) vibrations of MoS_2 atoms, respectively (see Fig. S3a in the ESI†). For CuPc, the most intense Raman bands were observed at 1144, 1345, 1454, and 1531 cm^{-1} for the pyrrole groups, phthalocyanine, the C–N bond, and the C–C bond, respectively (Fig. S3b in the ESI†). The CuPc/MoS_2 film was further examined by X-ray photoelectron spectroscopy (XPS). The XPS scans on a MoS_2 flake confirmed the chemical

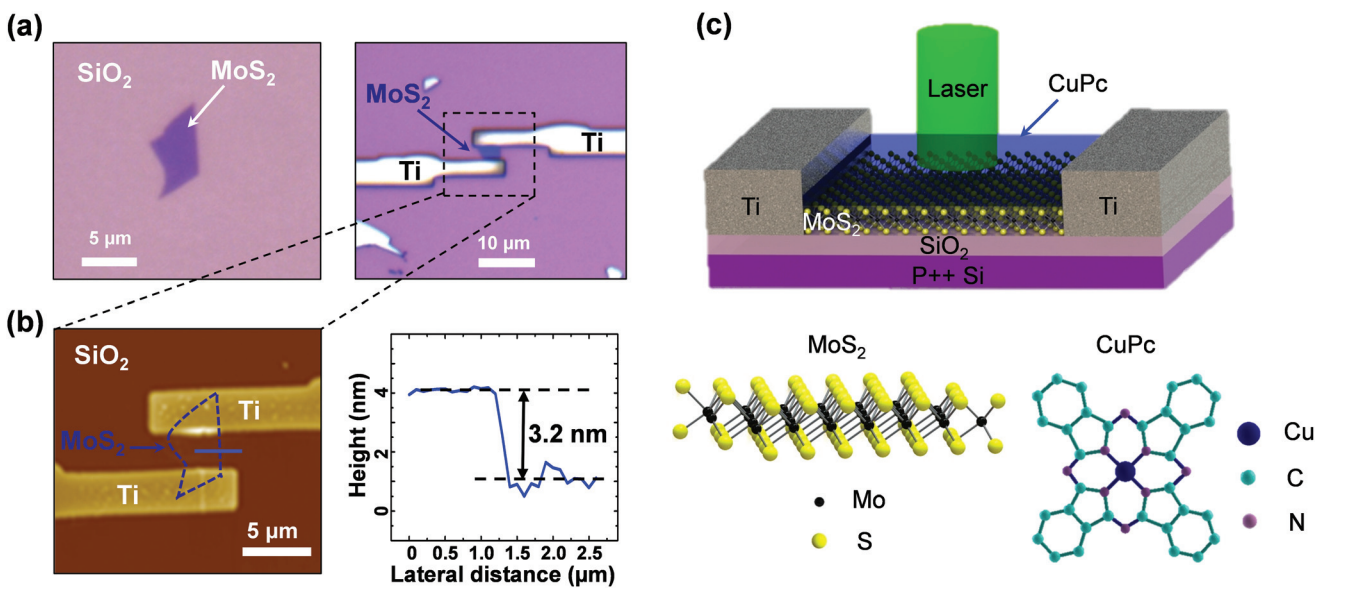

Fig. 1 (a) Optical images of a MoS_2 flake before (left) and after (right) Ti electrodes were deposited. (b) AFM image (left) of a fabricated MoS_2 FET device using the MoS_2 flake shown in (a, b). A cross-sectional topographic profile (right) indicated by the blue line shown in the AFM image. Dashed line indicates the MoS_2 flake. (c) Schematic of CuPc/MoS_2 device illuminated by a laser. The molecular structures of the MoS_2 and CuPc are also shown.

bonding states of the Mo and S. Also we compared the core-level peaks of Mo and S in the MoS_2 flake and CuPc/MoS_2 film (see Fig. S4a and S4b in the ESI†). And, the CuPc layer showed element peaks of Cu, N and C in the XPS spectra (see Fig. S4c–S4e in the ESI†).

Shift of the threshold voltage

Fig. 2a shows the transfer characteristics (*i.e.*, drain–source current *versus* gate voltage, I_{DS}–V_G) of a MoS_2 FET device upon which CuPc layers with different thicknesses, varying from 1 to 10 nm, were deposited. The thickness of the CuPc layer was accurately controlled by a thermal evaporator with few angstroms error (see Fig. S5 in the ESI†). The data were measured at a fixed source–drain voltage (V_{DS}) of 0.1 V in a vacuum ($\sim 10^{-4}$ Torr) at room temperature. The pristine MoS_2 device (labeled with w/o CuPc, the device before the CuPc layers were coated) exhibited n-type FET behavior. In our work, the room temperature mobility (μ) of the MoS_2 FET was found to be as low as ~ 1.67 cm^2 V^{-1} s^{-1}. Here, the mobility was estimated by using the formula $\mu = (dI_{DS}/dV_G) \times [L/(WC_iV_{DS})]$, where W ($\sim$4.3 μm) is the channel width, L ($\sim$2.4 μm) the channel length, and $C_i = \varepsilon_0\varepsilon_r/d \sim 1.3 \times 10^{-4}$ F m^{-2} the capacitance between the MoS_2 and p++ Si back gate per unit area. Here, ε_0 is the vacuum permittivity, ε_r ($\sim$3.9) is the dielectric constant of the SiO_2 dielectric, and d is the thickness (270 nm) of the SiO_2 layer. The on/off current ratio of this pristine MoS_2 FET was found to be $\sim 10^6$. The low mobility of MoS_2 FET devices is mainly due to the charge traps or adsorbates at the interface between the substrate and the MoS_2 layer.[1,7] It should be noted that the CuPc layer was coated on the MoS_2 layer after Ti/MoS_2 ohmic contacts were formed, and we measured the electrical properties of the devices in a vacuum ($\sim 10^{-4}$ Torr). These indicate that the lower mobility is not due to the contact properties of Ti/MoS_2, instead we suspect that low mobility of our devices was mainly attributed to the charge traps or adsorbates at the interface between the SiO_2 substrate and the MoS_2 layer.

The transfer characteristics of the same MoS_2 FET device after the CuPc layers were deposited on the MoS_2 surface are also plotted in Fig. 2a. When the CuPc layer was deposited, the channel currents at the positive gate voltages decreased, and the threshold voltage shifted towards the positive gate voltage direction compared with the case prior to the CuPc coating and as the thickness of the CuPc layer increased (see inset graph in Fig. 2a). Throughout the process, we measured the transfer characteristics of the MoS_2 FET devices systematically each time we coated the CuPc layers to increase their thickness. For example, the threshold voltage of the pristine MoS_2 FET was $\sim$0.45 V, and it shifted from 5.91 to 12.84 V when the thickness of the CuPc layers increased from 1 nm to 10 nm. The channel current of the pristine MoS_2 FET was 1.46×10^{-7} A measured at V_G = 40 V and V_{DS} = 0.1 V. The channel current

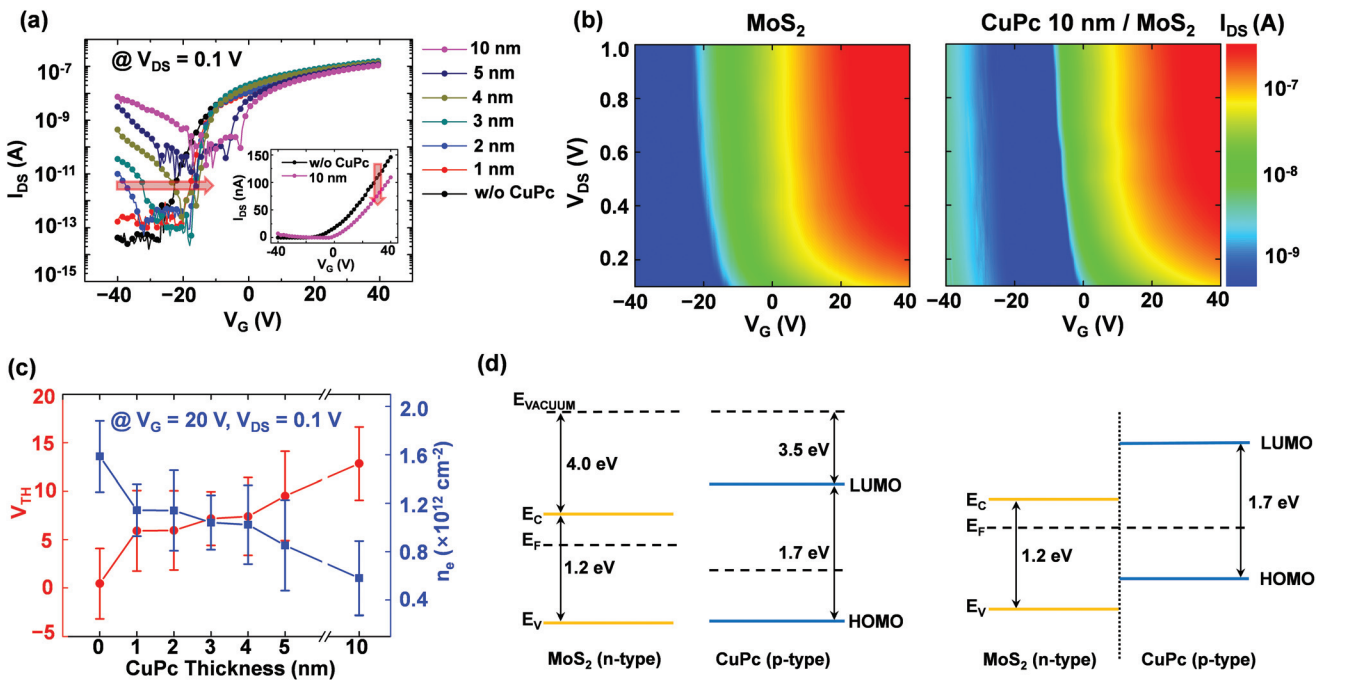

Fig. 2 (a) I_{DS}–V_G curves on the semilogarithmic scale of the MoS_2 devices without (labeled with "w/o CuPc") and with CuPc layers of various thicknesses (1, 2, 3, 4, 5, and 10 nm) measured at a fixed V_{DS} = 0.1 V. Inset is a linear plot of I_{DS}–V_G curves for a pristine MoS_2 device without a CuPc layer and a 10 nm-thick CuPc/MoS_2 hybrid device. Arrows indicate shifts in threshold voltages and currents. (b) The contour plots of I_{DS} as a function of V_G and V_{DS} for a (left) pristine MoS_2 device and (right) 10 nm-thick CuPc/MoS_2 devices. (c) The threshold voltage and electron carrier concentrations for a pristine MoS_2 device and CuPc/MoS_2 devices as a function of the thickness of the CuPc layers. (d) Schematics of energy band alignment of CuPc/MoS_2 (left) before and (right) after stacking on each other.

decreased from 1.25×10^{-7} to 1.09×10^{-7} A when the thickness of the CuPc layers increased from 1 nm to 10 nm. Note that we also studied the MoS_2 FET by stacking thicker CuPc layers (from 10 to 30 nm), and we observed consistent results, *i.e.*, the current at the positive gate voltage range decreased, and the threshold voltage shifted towards the positive gate voltage direction (see Fig. S6 in the ESI†).

Additionally, it was observed that the current in the negative gate voltage range (for example, at $V_G = -40$ V) increased upon increasing the thickness of the CuPc layers. The threshold voltage shift and current change in the MoS_2 FETs after the CuPc treatment can be seen more clearly in the contour plots of the current. Fig. 2b displays the contour plots of the channel current as a function of V_G and V_{DS} for the MoS_2 FET device. These plots were obtained from the transfer characteristic curves measured within the range of 0.1 to 1 V for V_{DS} and −40 to 40 V for V_G before (left) and after (right) the 10 nm-thick CuPc layer stacking. Here, one can clearly see that the channel current decreased at the positive gate voltages and that the threshold voltage shifted in the positive gate voltage direction with increasing thickness of the CuPc layer. The right panel of Fig. 2b representing the channel current of the CuPc/MoS_2 device also shows the hole conducting region near the high negative gate voltage. These phenomena are due to charge diffusion at the interface between the MoS_2 and CuPc layer. The mechanism of these phenomena will be explained in detail later.

Fig. 2c summarizes the threshold voltage values of all the MoS_2 FET devices that were characterized with and without CuPc layers of different thickness. The error bars in this plot indicate the standard deviations of the threshold voltages from at least four different MoS_2 FET devices at each CuPc layer thickness. One can see that the threshold voltages shifted in the positive gate voltage direction with increasing thickness of the CuPc layers. We estimated the electron carrier concentration of all the MoS_2 FET devices, and the results are also plotted in Fig. 2c. Here, the electron concentration (n_e) was calculated by using the formula $n_e = Q/e = C_g \times |V_G - V_{TH}|/e$, where C_g is the capacitance of the SiO_2 dielectric layer, and e is the elementary charge. In the calculation, we arbitrarily chose the gate voltage $V_G = 20$ V, at which none of the transfer characteristics were in the off condition. The electron concentration at $V_G = 20$ V and $V_{DS} = 0.1$ V decreased with increasing thickness of the CuPc layers.

The observation of the threshold voltage shift and the current decrease in the positive gate voltage range can be explained by the effect of CuPc on MoS_2. CuPc is known to show a p-type organic semiconductor characteristic. Therefore, when a p-type CuPc layer is stacked on an n-type MoS_2, the electrons in MoS_2 can recombine with holes in the CuPc layer at the interface. In case of stacking the CuPc thicker, more electrons can recombine, which is responsible for the threshold voltage shift and the current decrease in the positive gate voltage range (see Fig. 2d). Such carrier recombination at the interface between MoS_2 and CuPc layers results in a reduction of the electron carrier concentration in the MoS_2 channel layer and threshold voltage shift in the FET device. In our work, the carrier mobility in the MoS_2 channel layer is not changed much on increasing the thickness of the CuPc layer (see Fig. S7 in the ESI†). At the same time, the current increased in the negative gate voltage range due to the hole conduction through the p-type CuPc layer between the source and drain electrodes. This charge transfer behavior will become more significant when the thickness of the CuPc layer increases on the MoS_2 film.

Enhancement of photoresponsive characteristics

We studied the photoresponsive characteristics of the CuPc/MoS_2 hybrid devices under different light intensity (the power of the laser source) conditions (0.03, 0.05, 10, 25, 35, and 40 mW), and the results are shown in Fig. 3a. In this figure, the data in black (labeled as Dark) were obtained in the dark without laser illumination. Because the energy of the incident light (~2.38 eV, 520 nm wavelength) is greater than the band gap energy of the multilayer MoS_2 (~1.2 eV) and the CuPc layer (~1.7 eV), it can be absorbed and can generate electron–hole pairs in both the CuPc layer and the MoS_2 channel film. In the case of a pristine MoS_2 FET without the CuPc layer, the incident light is absorbed by the MoS_2 film, and the photo-generated electron–hole pairs contribute to the increasing current in the MoS_2 FETs. On the other hand, in the case of hybrid CuPc/MoS_2 FET devices, the incident light is absorbed by both the CuPc layer and the MoS_2 film. The photo-generated electron–hole pairs in the CuPc layer are separated at the interface between the p-type CuPc layer and the n-type MoS_2. Then, the electrons migrating from the CuPc layer to the MoS_2 contribute additional current. Note that to check whether the electron–hole pairs can be generated in the CuPc layer by the incident light, we measured the photoconductive properties of the CuPc-only FET without the MoS_2 film in the device structure. We observed that the incident light indeed generated the electron–hole pairs in the CuPc layer (see Fig. S8 in the ESI†).

From the experimental results (Fig. 3a), we observed two main phenomena. First, the photoinduced current level increased with increasing light intensity for both the pristine MoS_2 and hybrid CuPc/MoS_2 FETs. This result is simply due to a greater generation of electron–hole pairs by the more intense light. Additionally, the photoinduced current in the CuPc/MoS_2 FET was higher than that in the pristine MoS_2 FET due to the photo-generated electrons in the CuPc layer transferring from the CuPc layer to the MoS_2, producing additional current. These phenomena are summarized in Fig. 3b, where we plotted the photoinduced current of the pristine MoS_2 and CuPc/MoS_2 FETs measured at $V_G = -40$ V and $V_{DS} = 0.1$ V in the dark and under 520 nm laser illumination at different laser intensities. For example, the photocurrent (38.1 nA) of the CuPc/MoS_2 FET was approximately an order of magnitude higher than that (3.13 nA) of the pristine MoS_2 FET at 40 mW laser illumination at $V_G = -40$ V.

Fig. 3c shows the photoresponsive data of the pristine MoS_2 and CuPc (2 nm-thick layer)/MoS_2 FETs measured at V_G = (−40 V and VVDS = 0.1 V in the darkness and under laser

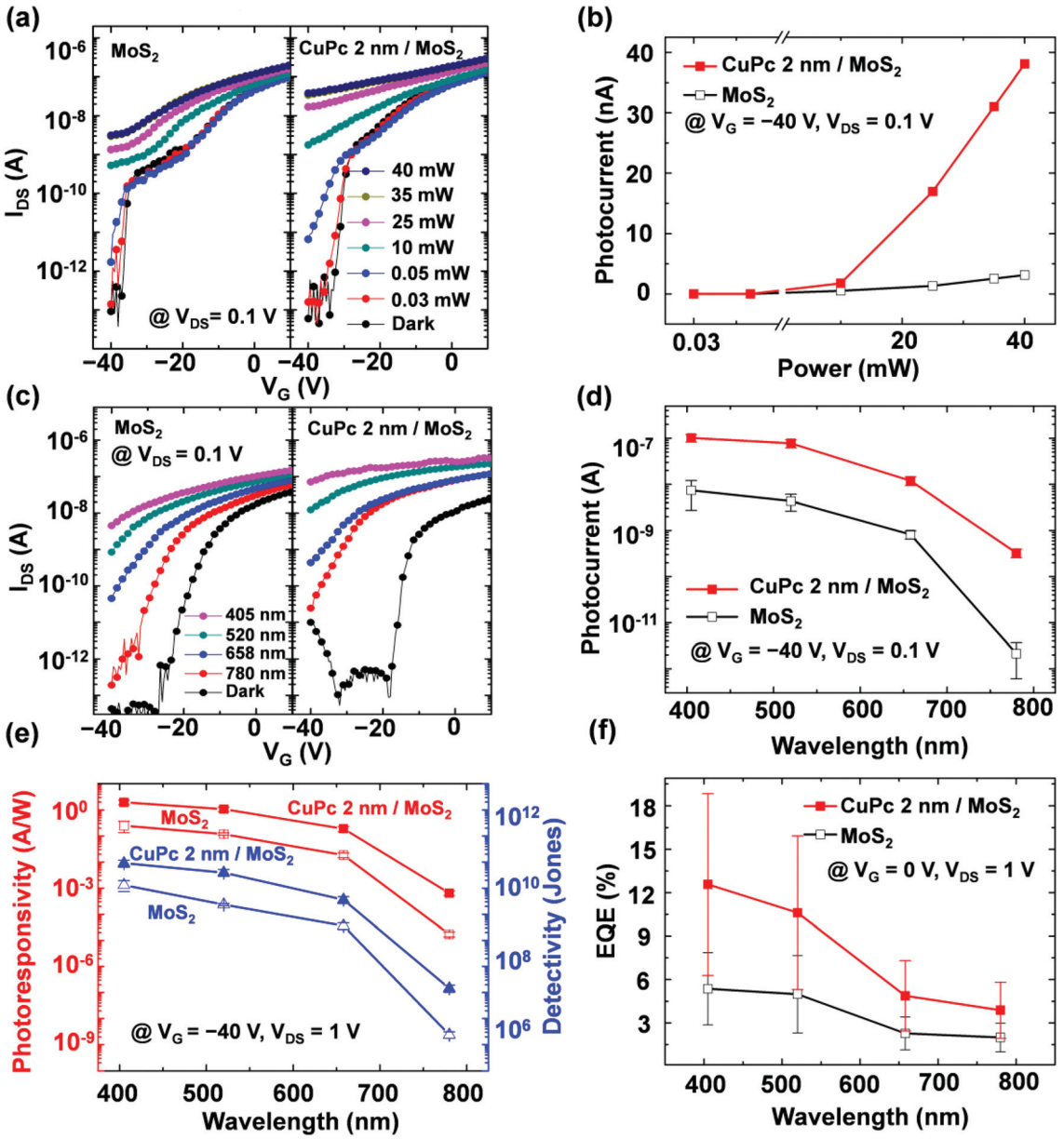

Fig. 3 (a) I_{DS}–V_G curves of pristine MoS_2 and 2 nm-thick CuPc/MoS_2 photodetectors measured at a fixed V_{DS} = 0.1 V under dark and illuminated conditions (wavelength = 520 nm) at different laser intensities. (b) Photocurrent of pristine MoS_2 and CuPc/MoS_2 photodetectors measured at V_G = −40 V and V_{DS} = 0.1 V as a function of the laser intensity. (c) I_{DS}–V_G curves of pristine MoS_2 and CuPc/MoS_2 photodetectors measured under dark and light illumination conditions at different wavelengths and a fixed laser intensity (40 mW). (d) Photocurrent, (e) photoresponsivity and detectivity, and (f) external quantum efficiency (EQE) of pristine MoS_2 and CuPc/MoS_2 photodetectors as a function of the wavelength of the illumination.

illumination with different wavelengths and a fixed intensity of 40 mW. Four different laser wavelengths (405, 520, 658, and 780 nm) were used for this experiment, and all of them exceeded the band gap energy values of the multilayer MoS_2 and CuPc. The photoinduced current increased as the wavelength of the incident light became shorter, indicating that the incident light having energy larger than the energy gap of the CuPc and MoS_2 can create electron–hole pairs more easily. Moreover, similar to the results of Fig. 3a and b, we observed that the photocurrent from the CuPc/MoS_2 hybrid device was higher than that of the pristine MoS_2 device by an order of magnitude throughout the wavelength ranges (Fig. 3d).

The performances of photodetectors are often evaluated using photoresponsivity, detectivity, and external quantum efficiency. The photoresponsivity (R) can be estimated from the formula $R = I_{Ph}/P_{Light}$, where I_{Ph} is the photocurrent and P_{Light} is the intensity of incident light. In the calculation, we only considered the active area of the incident flux of laser illumination (with a laser spot radius of 0.5×10^{-3} m). The calculated photoresponsivity values for the pristine MoS_2 and CuPc

(2 nm-thick layer)/MoS_2 phototransistors are plotted in Fig. 3e. One can see that the photoresponsivity increased with shorter wavelengths of the illuminating light and was higher for the CuPc/MoS_2 than the pristine MoS_2 devices. Moreover, the detectivity (D^*) parameter can be estimated using $D^* = (RA_D{}^{1/2})/(2eI_D)^{1/2}$, where A_D is the effective detection area, I_D is the unilluminated current, and e is the elementary charge (1.6×10^{-19} C). The determined detectivity values of the CuPc/MoS_2 and pristine MoS_2 photodetectors are plotted in Fig. 3e. The results in Fig. 3e indicate that both the photoresponsivity and detectivity of the MoS_2 devices increased by roughly an order of magnitude with stacking of the CuPc layer on the MoS_2 surface. From the photocurrent values, we estimated the external quantum efficiency (EQE), which is the efficiency of converting electrons according to incident photons (Fig. 3f). The EQE is defined as EQE = $(I_{Ph}/e)/(P_{Light}/h\nu)$, where $h\nu$ is the photon energy. The pristine MoS_2 photodetectors displayed an R of 0.25 A W^{-1}, a D^* of 1.49×10^{10} Jones (measured at V_G = −40 V and V_{DS} = 1 V), and an EQE of 5.36% under 405 nm illumination at 40 mW intensity (measured at V_G = 0 V and V_{DS} = 1 V). In contrast, the CuPc/MoS_2 hybrid photodetectors exhibited an R of 1.98 A W^{-1}, a D^* of 6.11×10^{10} Jones, and an EQE of 12.57% under the same measurement conditions as the pristine MoS_2 devices. With these photodetection results shown in Fig. 3, we can confirm that the CuPc/MoS_2 hybrid devices exhibited a better photodetection capability than the pristine MoS_2 devices in the broad wavelength and optical intensity ranges. In addition, we investigated the gate voltage dependence of the photoresponsive characteristics (see Fig. S9 in the ESI†). We found that the photoresponsive properties increased as the increasing gate voltage, which results in the increase of electron carriers in the MoS_2 layer and the reduction of charge recombination.

Optical properties with different CuPc layers

Fig. 4a shows the photo-switching data before and after the MoS_2 FET devices were deposited with CuPc layers of different thicknesses (1, 2, 3, 4, 5, and 10 nm). Note that in order to clearly compare and emphasize differences in the time-dependent photocurrent behavior, the photocurrents were normalized, *i.e.*, the light-off currents in the dark of each curve were shifted by an equal distance (15 nA) in the y-axis. The white areas represent the light-off current of the devices (labeled "light off"), and the cyan areas indicate the light-on current of the devices under 520 nm illumination (labeled "light on"). We observed that there are striking differences in the photocurrent ratio (a photocurrent-to-dark condition ratio) as a function of the thickness of the CuPc layer while the light turns off and on. From Fig. 4b, it is clearly seen that the photocurrent and photoresponsivity of the CuPc/MoS_2 hybrid devices strongly depended on the thickness of the CuPc layers on the MoS_2, and in particular the device conditions with the 2 nm-thick CuPc layer showed the largest photocurrent and photoresponsivity. This indicates that the high efficient performance between the light absorption and photodetection in the CuPc/MoS_2 heterostructures can be obtained by optimizing the appropriate thickness of a p-type organic layer due to the increase of charge recombination at the interface with increasing hole carriers in the CuPc layer. The photo-generated electrons in the CuPc layer can assist the increase of photocurrent in the hybrid device. However, the increase of hole carrier density in the thicker CuPc layer than 2 nm (see Fig. S8 in the ESI†) leads to the increase of recombination with electrons in the MoS_2 layer at the interface (see Fig. 2 and S6†), which can cause the reduction of photoresponsivity. After the thin MoS_2 and CuPc layers form a junction, the excitons from the CuPc layer are generated upon light illumination. The photo-generated electrons in the lowest unoccupied molecular orbital (LUMO) level of the CuPc move to the interface and then transfer to the MoS_2 layer (black arrows in Fig. 4c and d) due to the energy alignment (*i.e.*, LUMO of the CuPc is higher than the conduction band minimum of the MoS_2). In contrast, the photo-generated holes in the highest occupied molecular orbital (HOMO) level of the CuPc could not move to MoS_2 due to the larger barrier. Here, the interlayer recombination processes can occur at the interface between the thin MoS_2 and CuPc layers. These processes are described as trap-assisted recombination (known as Shockley–Read–Hall recombination) by inelastic tunneling of carriers into trap states in the forbidden gap (marked by the blue arrows in Fig. 4c and d) and as Langevin recombination of the electron–hole carriers *via* the Coulomb interaction (marked by the red allows in Fig. 4c and d) across the interface.[40–43] Both interlayer recombination processes are proportional to the density of the major charge carriers in the MoS_2 and CuPc layers.[40,43] Interestingly, in Fig. 2a and S8 of the ESI,† the current in the negative gate voltage range for the CuPc/MoS_2 hybrid and CuPc-alone FET devices increased with increasing thickness of the CuPc layers, so that the p-type behavior became stronger. This indicates that as the thickness of the CuPc layer increases, the density of hole carriers in the CuPc layer increases, which results in the decrease in the energy difference between the Fermi level and HOMO level of the CuPc (Fig. 4c and d) with increased CuPc layer thickness. Therefore, the thickness dependence of the density of hole carriers can strongly affect the interlayer recombinations for the CuPc/MoS_2 devices. Compared with the smaller energy difference (ΔE_{small}) of thicker CuPc (Fig. 4d), the total number of majority carriers that cause interlayer recombinations is relatively smaller due to the larger energy difference (ΔE_{large}) in the case of the junction between the MoS_2 and the relatively thinner CuPc layer, leading to the stronger enhancement of photodetection performance (Fig. 4c). In addition, when the CuPc layer is much thicker than the exciton diffusion length (~1.6 nm),[44] the photo-generated electron and hole pairs will recombine before they separate and will not contribute to the photocurrent. Therefore, as an overall effect, such as the contribution of photo-generated electrons in the CuPc layer, recombination processes, and exciton diffusion length, the relatively thinner CuPc/MoS_2 devices (near the 2 nm CuPc) exhibited higher photoresponsivity than the relatively thicker CuPc/MoS_2 devices. Finally, the time-resolved photocurrent of 2 nm-thick CuPc/MoS_2 and pristine MoS_2

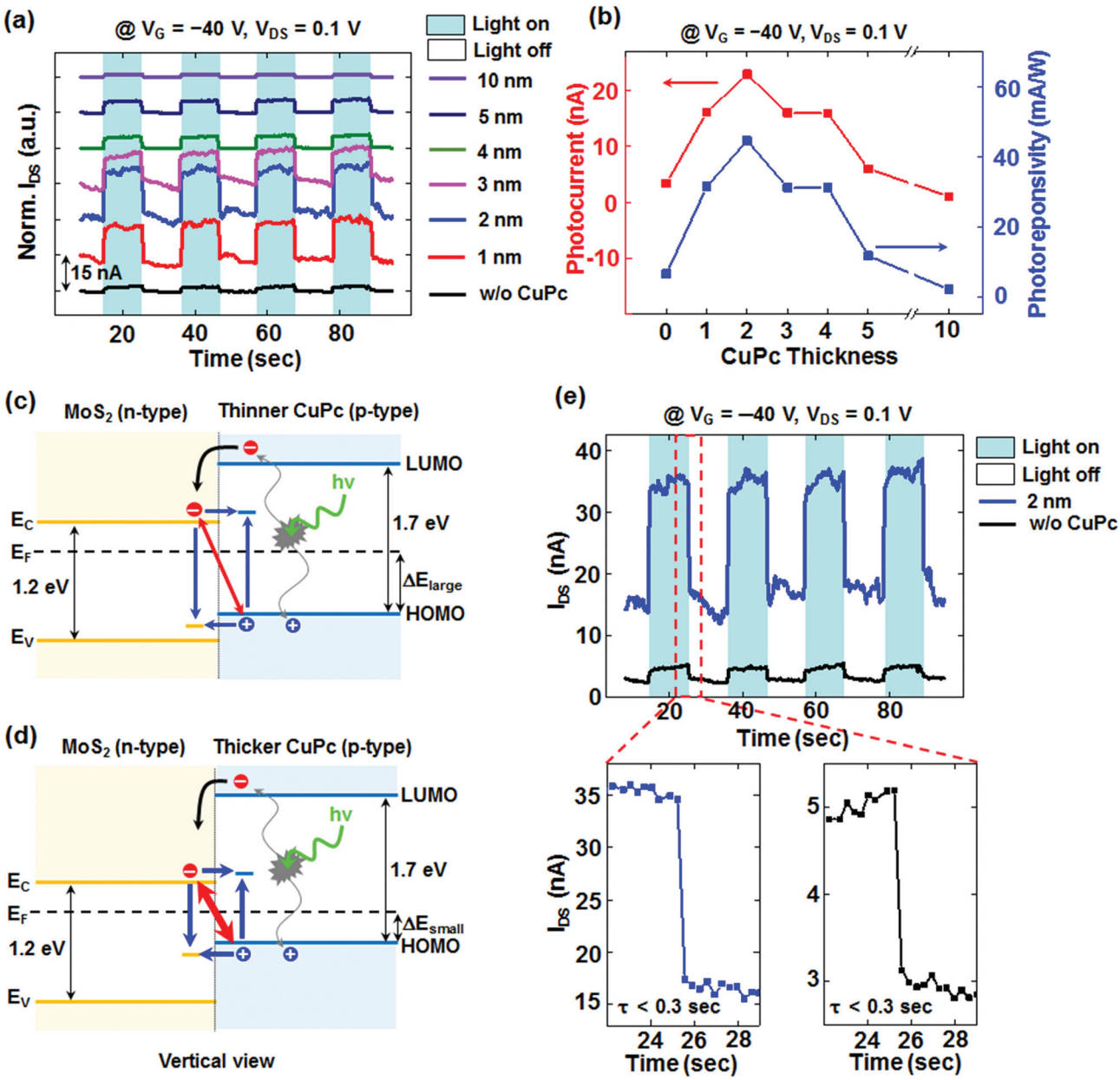

Fig. 4 (a) Normalized photo-switching data of pristine MoS_2 and CuPc/MoS_2 photodetectors with different CuPc layer thicknesses (1, 2, 3, 4, 5, and 10 nm) measured at V_G = −40 V and V_{DS} = 0.1 V while a light (wavelength = 520 nm, intensity = 40 mW) was on and off. (b) Photocurrent and photoresponsivity of devices *versus* the CuPc layer thickness. (c, d) Energy band diagrams of (c) a relatively thinner CuPc/MoS_2 device and (d) a relatively thicker CuPc/MoS_2 device. Blue lines and red lines indicate SHR and Langevin recombination processes, respectively. (e) Time-resolved photocurrent data of 2 nm-thick CuPc/MoS_2 and MoS_2 devices show that both devices exhibited short decay times (τ < 0.3 s).

devices showed sufficiently short typical decay times (τ < 0.3 s). The decay time might not be clearly measured due to the limit of equipment capacity but which is faster than previously reported MoS_2 devices.[27]

Conclusions

We investigated the photoresponsive properties of MoS_2 FETs when stacking a p-type organic semiconductor (CuPc) layer on the MoS_2 surface. The CuPc/MoS_2 hybrid devices exhibited better performance as photodetectors compared with the pristine MoS_2 FETs that did not contain CuPc layers, due to the transfer of photo-generated charge carriers from the CuPc to the MoS_2. Furthermore, we observed that the photoresponsive properties of the CuPc/MoS_2 devices depended on the thickness of the CuPc layer. The device with a relatively thinner CuPc layer exhibited a better photodetection performance than that with a relatively thicker CuPc layer, which can be

explained by the CuPc layer thickness-dependent interlayer recombination processes across the CuPc/MoS_2 interface. We found that the 2 nm-thick CuPc/MoS_2 device presented the highest photodetection performance, with a photoresponsivity of ~1.98 A W^{-1}, a detectivity of ~6.11 × 10^{10} Jones, and an external quantum efficiency of ~12.57%. This study suggests an approach to creating MoS_2-based heterostructures by stacking with p-type organic semiconductors, resulting in an efficient photodetecting device.

Experimental section

Materials and fabrication of MoS_2 FET devices

The MoS_2 FET devices were fabricated using multilayer MoS_2 flakes that were exfoliated from a bulk MoS_2 crystal using the micromechanical exfoliation method. The multilayer MoS_2 flakes were then transferred to 270 nm-thick SiO_2 on a high doped p++ Si wafer (resistivity ~5 × 10^{-3} Ω cm^{-1}) that can be used as a back gate. After finding the location of the target MoS_2 flakes using an optical microscope, the height of the MoS_2 flakes was measured using an AFM system (NX 10 AFM, Park Systems). To create electrode patterns, we spin-coated double resist layers—methyl methacrylate (9% concentration in ethyl lactate) and polymethyl methacrylate (5% concentration in anisole; PMMA 950K A5) at 4000 rpm of each resist layer. The samples were baked twice at 180 °C for 90 s on a hot plate after spin-coating each resist layer. We used an electron beam lithography system (JSM-6510, JEOL) to pattern the source and drain electrodes. Pattern development was performed using a MIBK/IPA (1 : 3) solution for 50 s. The electrodes were deposited with an electron-beam evaporator system (KVE-2004L, Korea Vacuum Tech). Finally, the devices were annealed under 100 sccm Ar flow at 200 °C for 2 h.

Fabrication of CuPc/MoS_2 photodetectors

To create the CuPc/MoS_2 hybrid structure, copper phthalocyanine (Lumtec (Sublimed product)) was deposited on the MoS_2 surface using a thermal evaporator system (GVTE1000, GV-Tech).

Device characterization

All electrical characteristics of the devices were measured using a probe station (JANIS, ST-500) and a semiconductor parameter analyzer (Keithley 4200-SCS). The photoresponsive characteristics of the devices were measured under laser (purchased from Su Semiconductor, model MDE5240 V) illumination at various wavelengths.

Acknowledgements

The authors appreciate the financial support of the National Creative Research Laboratory program (Grant No. 2012026372) through the National Research Foundation of Korea (NRF), funded by the Korean Ministry of Science, ICT & Future Planning. W.-K. H. acknowledges the financial support from the Basic Science Research Program through the NRF (Grant No. NRF-2013-R1A1A2009884), funded by the Korean Ministry of Education.

Notes and references

1 K. Novoselov, D. Jiang, F. Schedin, T. Booth, V. V. Khotkevich, S. V. Morozov and A. K. Geim, *Proc. Natl. Acad. Sci. U. S. A.*, 2005, **102**, 10451.
2 D. Jariwala, V. K. Sangwan, L. J. Lauhon, T. J. Mark and M. C. Hersam, *ACS Nano*, 2014, **8**, 1102.
3 R. Mas-Balleste, C. Gomez-Navarro, J. Gomez-Herrero and F. Zamora, *Nanoscale*, 2011, **3**, 20.
4 Q. H. Wang, K. Kalantar-Zadeh, A. Kis, J. N. Coleman and M. S. Strano, *Nat. Nanotechnol.*, 2012, **7**, 699.
5 S. Lei, F. Wen, B. Li, Q. Wang, Y. Huang, Y. Gong, Y. He, P. Dong, J. Bellah, A. George, J. Lou, N. J. Halas, R. Vajtai and P. M. Ajayan, *Nano Lett.*, 2015, **15**, 259.
6 W. Park, J. Baik, T.-Y. Kim, K. Cho, W.-K. Hong, H. J. Shin and T. Lee, *ACS Nano*, 2013, **8**, 4961.
7 B. Radisavljevic, A. Radenovic, J. Brivio, V. Giacometti and A. Kis, *Nat. Nanotechnol.*, 2011, **6**, 147.
8 H. Liu, A. T. Neal and P. D. Ye, *ACS Nano*, 2012, **6**, 8563.
9 S. Kim, A. Konar, W.-S. Hwang, J. H. Lee, J. Lee, J. Yang, C. Jung, H. Kim, J.-B. Yoo, J.-Y. Choi, Y. W. Jin, S. Y. Lee, D. Jena, W. Choi and K. Kim, *Nat. Commun.*, 2012, **3**, 1011.
10 A. M. Goldberg, A. R. Beal, F. A. Levy and E. A. Davis, *Philos. Mag.*, 1975, **32**, 367.
11 K. F. Mak, C. Lee, J. Hone, J. Shan and T. F. Heinz, *Phys. Rev. Lett.*, 2010, **105**, 136805.
12 A. Splendiani, L. Sun, Y. Zhang, T. Li, J. Kim, C.-Y. Chim, G. Galli and F. Wang, *Nano Lett.*, 2010, **10**, 1271.
13 H. S. Lee, S.-W. Min, Y.-G. Chang, M. K. Park, T. Nam, H. Kim, J. H. Kim, S. Ryu and S. Im, *Nano Lett.*, 2012, **12**, 3695.
14 L. Yang, X. Cui, J. Zhang, K. Wang, M. Shen, S. Zeng, S. A. Dayeh, L. Feng and B. Xiang, *Sci. Rep.*, 2014, **4**, 5649.
15 S. Chuang, C. Battaglia, A. Azcatl, S. McDonnell, J. S. Kang, X. Yin, M. Tosun, R. Kapadia, H. Fang, R. M. Wallace and A. Javey, *Nano Lett.*, 2014, **14**, 1337.
16 Y. Zhang, J. Ye, Y. Matsuhashi and Y. Iwasa, *Nano Lett.*, 2012, **12**, 1136.
17 H. Li, Z. Yin, Q. He, H. Li, X. Huang, G. Lu, D. W. H. Fam, A. I. Y. Tok, Q. Zhang and H. Zhang, *Small*, 2012, **8**, 63.
18 K. Cho, W. Park, J. Park, H. Jeong, J. Jang, T.-Y. Kim, W.-K. Hong, S. Hong and T. Lee, *ACS Nano*, 2013, **7**, 7751.
19 K. Roy, M. Padmanabhan, S. Goswami, T. P. Sai, G. Ramalingam, S. Raghavan and A. Ghosh, *Nat. Nanotechnol.*, 2013, **8**, 826.
20 S. Bertolazzi, D. Krasnozhon and A. Kis, *ACS Nano*, 2013, **7**, 3246.
21 B. Radisavljevic, M. B. Whitwick and A. Kis, *ACS Nano*, 2011, **5**, 9934.

22 H. Wang, L. Yu, Y.-H. Lee, Y. Shi, A. Hsu, M. L. Chin, L.-J. Li, M. Dubey, J. Kong and T. Palacios, *Nano Lett.*, 2012, **12**, 4674.
23 B. Liu, L. Chen, G. Liu, A. N. Abbas, M. Fathi and C. Zhou, *ACS Nano*, 2014, **8**, 5304.
24 D. Sarkar, W. Liu, X. Xie, A. C. Anselmo, S. Mitragotri and K. Banerjee, *ACS Nano*, 2014, **8**, 3992.
25 Z. Yin, H. Li, H. Li, L. Jiang, Y. Shi, Y. Sun, G. Lu, Q. Zhang, X. Chen and H. Zhang, *ACS Nano*, 2011, **6**, 74.
26 T. Mueller, F. Xia and P. Avouris, *Nat. Photonics*, 2010, **4**, 297.
27 O. Lopez-Sanchez, D. Lembke, M. Kayci, A. Radenovic and A. Kis, *Nat. Nanotechnol.*, 2013, **8**, 497.
28 W. Choi, M. Y. Cho, A. Konar, J. H. Lee, G. B. Cha, S. C. Hong, S. Kim, J. Kim, D. Jena, J. Joo and S. Kim, *Adv. Mater.*, 2012, **24**, 5832.
29 D.-S. Tsai, K.-K. Liu, D.-H. Lien, M.-L. Tsai, C.-F. Kang, C.-A. Lin, L.-J. Li and J.-H. He, *ACS Nano*, 2013, **7**, 3905.
30 D. Jariwala, V. K. Sangwan, C.-C. Wu, P. L. Prabhumirashi, M. L. Geier, T. J. Marks, L. J. Lauhon and M. C. Hersam, *Proc. Natl. Acad. Sci. U. S. A.*, 2013, **110**, 18076.
31 Y. Li, C.-Y. Xu, J.-Y. Wang and L. Zhen, *Sci. Rep.*, 2014, **4**, 7186.
32 J. Schornbaum, B. Winter, S. P. Schießl, F. Gannott, G. Katsukis, D. M. Guldi, E. Spiecker and J. Zaumseil, *Adv. Funct. Mater.*, 2014, **24**, 5798.
33 S. H. Yu, Y. Lee, S. K. Jang, J. Kang, J. Jeon, C. Lee, J. Y. Lee, H. Kim, E. Hwang, S. Lee and J. H. Cho, *ACS Nano*, 2014, **8**, 8285.
34 W. Zhang, C.-P. Chuu, J.-K. Huang, C.-H. Chen, M.-L. Tsai, Y.-H. Chang, C.-T. Liang, Y.-Z. Chen, Y.-L. Chueh, J.-H. He, M.-Y. Chou and L.-J. Li, *Sci. Rep.*, 2014, **4**, 3826.
35 D. Kufer, I. Nikitskiy, T. Lasanta, G. Navickaite, F. H. L. Koppens and G. Konstantatos, *Adv. Mater.*, 2015, **27**, 176.
36 Z. Bao, A. J. Lovinger and A. Dodabalapur, *Appl. Phys. Lett.*, 1996, **69**, 3066.
37 K. K. Okudaira, S. Hasegawa, H. Ishii, K. Seki, Y. Harada and N. Ueno, *J. Appl. Phys.*, 1999, **85**, 6453.
38 X. Ling, W. Fang, Y.-H. Lee, P. T. Araujo, X. Zhang, J. F. Rodriguez-Nieva, Y. Lin, J. Zhang, J. Kong and M. S. Dresselhaus, *Nano Lett.*, 2014, **14**, 3033.
39 Q. Hao, P. Lijia, Y. Zongni, L. Junjin, S. Yi and W. Xinran, *Appl. Phys. Lett.*, 2012, **100**, 123104.
40 M. A. Green, *Solar cells: operating principles, technology, and system applications*, Prentice-Hall, Kensington, Australia, 1982, ch. 3.
41 N. Greenham and P. A. Bobbert, *Phys. Rev. B: Condens. Matter*, 2003, **68**, 245301.
42 G. Wetzelaer, M. Kuik, H. T. Nicolai and P. W. M. Blom, *Phys. Rev. B: Condens. Matter*, 2011, **83**, 165204.
43 C.-H. Lee, G.-H. Lee, A. M. van der Zande, W. Chen, Y. Li, M. Han, X. Cui, G. Arefe, C. Nuckolls, T. F. Heinz, J. Guo, J. Hone and P. Kim, *Nat. Nanotechnol.*, 2014, **9**, 676.
44 R. Signerski and G. Jarosz, *Photonics Lett. Pol.*, 2011, **3**, 107.